Nanoscale

RSC Publishing

PAPER

View Article Online
View Journal | View Issue

Cite this: *Nanoscale*, 2013, **5**, 5539

Strain-induced macroscopic magnetic anisotropy from smectic liquid-crystalline elastomer–maghemite nanoparticle hybrid nanocomposites†

Johannes M. Haberl,[a] Antoni Sánchez-Ferrer,[a] Adriana M. Mihut,‡[b] Hervé Dietsch,§[b] Ann M. Hirt[c] and Raffaele Mezzenga*[a]

Received 26th February 2013
Accepted 8th April 2013

DOI: 10.1039/c3nr01016c

www.rsc.org/nanoscale

We combine tensile strength analysis and X-ray scattering experiments to establish a detailed understanding of the microstructural coupling between liquid-crystalline elastomer (LCE) networks and embedded magnetic core–shell ellipsoidal nanoparticles (NPs). We study the structural and magnetic re-organization at different deformations and NP loadings, and the associated shape and magnetic memory features. In the quantitative analysis of a stretching process, the effect of the incorporated NPs on the smectic LCE is found to be prominent during the reorientation of the smectic domains and the softening of the nanocomposite. Under deformation, the soft response of the nanocomposite material allows the organization of the nanoparticles to yield a permanent macroscopically anisotropic magnetic material. Independent of the particle loading, the shape-memory properties and the smectic phase of the LCEs are preserved. Detailed studies on the magnetic properties demonstrate that the collective ensemble of individual particles is responsible for the macroscopic magnetic features of the nanocomposite.

Introduction

Liquid-crystalline elastomers (LCEs) combine the anisotropic properties of liquid crystals with the entropy elasticity of polymer networks, and give rise to various anisotropic properties such as the spontaneous macroscopic shape change at the phase transition[1] which is associated with property changes, similar to shape-memory alloys.[2] Several studies have shown a broad application potential for LCEs in smart actuators and sensors.[3–5] Nanocomposites of LCEs have been used to further expand the resulting applications beyond the traditional limits imposed by organic materials. In this context, LCE nanocomposites with MoO_{3-x} nanowires[6] or carbon black[7] have been introduced as conductive actuators. Gold nanoparticles were incorporated to enhance the thermo-mechanical response of such composites.[8] Moreover, to improve infrared and terahertz activity, carbon nanotubes were embedded into the matrix[9] and the composites were used as contactless strain sensors for infrared light.[10,11] Further efforts have also been made in the design of mechanically adaptive polymer nanocomposites, which change the tensile strength behaviour as a function of an external stimulus.[12,13] For example, in magnetic hybrid elastomers[14] and gels,[15] that were synthesized in the presence of an applied magnetic field to achieve chainlike-organized magnetic particles, mechanical experiments showed that a magnetic field coupled to the modulus of the material. Special interest was also devoted to the improvement of inductive activation of magnetic shape-memory nanocomposites and a "triple-shape effect" in recovery was achieved.[16] In a monodomain LCE nanocomposite, inductive heating of incorporated magnetite particles was used to heat the matrix beyond its transition temperature and to create an entropy-driven reversible actuator.[17] Magnetic domains without superparamagnetic relaxation were crucial for such success.[18] In our recent work, we presented the integration of covalently bonded ellipsoidal maghemite nanoparticles into a smectic LCE nanocomposite to build wireless strain sensors with a magnetic read-out of deformation.[19] Smectic LCEs with layered mesogen structures were related to shape-memory properties,[20] and similar behaviour was used to store magnetic information in the material, which enabled the very desirable feature of controlling magnetic properties using parameters typical of soft materials.[19]

The present study aims for an improvement of the understanding of the effects arising from nanoparticles incorporation into LCE host matrices. The incorporation of nanoparticles into

[a]*ETH Zürich, Department of Health Science and Technology, 8092 Zürich, Switzerland. E-mail: raffaele.mezzenga@hest.ethz.ch; Fax: +41-44-632-16-03; Tel: +41-44-632-91-40*

[b]*Adolphe Merkle Institute and Fribourg Center for Nanomaterials, University of Fribourg, 1723 Marly, Switzerland*

[c]*ETH Zürich, Department of Earth Science, 8092 Zürich, Switzerland*

† Electronic supplementary information (ESI) available: Fig. ESI-1: polarized optical microscopy images, Fig. ESI-2–4: supplementary X-ray data, Fig. ESI-5: FORC diagrams. See DOI: 10.1039/c3nr01016c

‡ Present Address: Physical Chemistry, Department of Chemistry, Lund University, 22100 Lund, Sweden.

§ Present Address: BASF SE, Formulation Platform, 67056 Ludwigshafen am Rhein, Germany.

organic networks to simply enhance the mechanical properties has been used for many years, *e.g.* in tyre production, but the mechanistic understanding is still under investigation.[21] Recently, different model approaches have been presented. These take into account a reduced polymer mobility in the vicinity of surfaces and interfaces which is explained on the basis of a glass-like behaviour.[22] Further extension leads to a three-zone model where the stabilisation is not only related to the α-relaxation (mostly frozen in the glass state), but also to a Rouse modes modification on extended length scales of about 10 nm from the particle surface.[23] Thus, the polymer of intermediate mobility can interconnect adjacent particles and strongly affect the material properties.[23–26] Moreover, aligned shape anisotropic particles have been shown to exert the strongest effect on material modulus.[27] One of the most successful models that describe the reinforcement effect of shape anisotropic objects is the Halpin–Tsai model.[28]

Using this approach, which combines both the simple and the inverted rule of mixture, we discuss the non-linear tensile behaviour of a polydomain LCE nanocomposite. For this purpose, six different LCEs were synthesized with magnetic NP loadings ranging from 0.5 to 10 w/w% and their behaviour was compared to a reference system without magnetic NPs. Results from stress–strain measurements showed an increase in the tensile modulus as a function of the NP content, and the particle effect on the different strain regions was evaluated. A mechanistic understanding of the reinforcement effect is developed, based on well-established models for the reorientation behaviour of LCE networks,[29] by combining X-ray diffraction measurements, differential scanning calorimetry and uniaxial stress–strain experiments. The incorporation of NPs into the LCE matrix is found to increase the amount of defects in the correlation of the LCEs, while mesogens and domains are aligned with respect to the stretching direction. Consequently, reduced mesogen and smectic layering orders were found with increasing particle loading, and the corresponding decrease in the transition enthalpy from the smectic to the isotropic phase was observed. We show that the effect of strain on the magnetic features and the microstructural reorganisation of such materials lead to a smart and responsive, magnetic-memory material which combines features of magnetic ellipsoidal NPs and a smectic LCE matrix.

Experimental

Materials

Iron(III) perchlorate hexahydrate, $Fe(ClO_4)_3 \cdot 6H_2O$, poly(vinylpyrrolidone) (PVP, 10 000 g mol^{-1}), tetramethylammonium hydroxide (TMAH) 25% solution in methanol, triethylene glycol, titanium(IV) isopropoxide, dibutyltin dilaurate were all provided by Sigma Aldrich; sodium dihydrogen phosphate monohydrate, $NaH_2PO_4 \cdot H_2O$, and urea were from Fluka; tetraethyl orthosilicate (TEOS) was from Merck; 3-aminopropyltriethoxysilane (APTES) was from ABCR, and all were used as received without further purification. Ultrapure water was used throughout the experiments, purified by a Milli-Q system. The crosslinker Basonat® HI-100 was kindly provided by BASF SE and used as received.

Synthesis

For the synthesis of the LCE nanocomposites, surface functionalized core–shell spindle-type NPs were synthesized having a major iron-oxide core axis of 310 ± 7 nm and a minor core axis of 55 ± 7 nm. The silica shell was 22 ± 4 nm along the major axis and 19 ± 2 nm along the minor axis.[19] The six LCEs were synthesized with different particle contents ranging from 0.5 to 10 w/w%, and a reference elastomer was prepared without any particle content. The involved synthetic steps follow closely our previous report,[19] and are outlined in Scheme 1 and discussed in detail in the ESI,† while all elastomer compositions are summarized in Table 1.

Methods and techniques

Transmission Electron Microscopy (TEM) images were taken with a Philips TEM (CM100) microscope at 80 kV. The films were ultramicrotomed using a Diatome diamond knife on a Reichert-Jung UltraCut E Microtome parallel to the stretching direction into sections of 80 nm thickness, and were transferred onto 600-mesh copper grids.

Differential Scanning Calorimetry (DSC) experiments were performed on a Mettler Toledo DSC1 calorimeter equipped with a Huber TC100 cooling system. Samples were encapsulated in

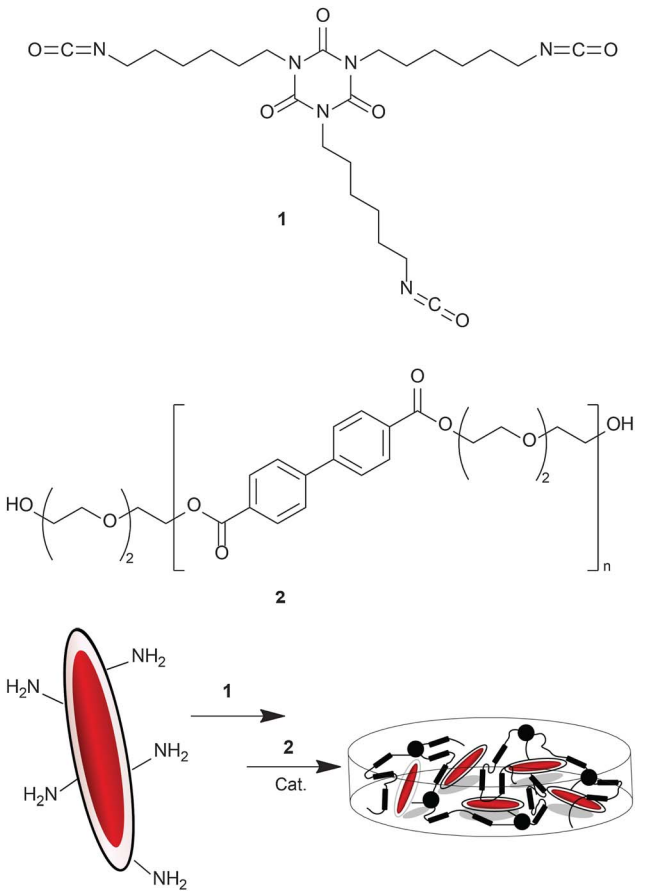

Scheme 1 Chemical structure of the crosslinker **1**, the liquid-crystalline polymer **2**, and the preparation of the liquid-crystalline elastomer–nanoparticle hybrids by solution casting.

Table 1 Magnetic nanoparticle content c_p and ϕ_p, gel content G, swelling ratio Q, glass-transition temperature T_g, and clearing temperature T_{SI} for the liquid-crystalline polymer P0 and the corresponding liquid-crystalline elastomers (E0–E10)

Sample	c_p (w/w%)	ϕ_p (v/v%)	G	Q	T_g (°C)	T_{SI} (°C)
P0	0.0	0.0	0.0	—	8	110
E0	0.0	0.0	0.79	9.5	15	75
E0.5	0.50	0.18	0.83	6.4	14	78
E1	1.0	0.35	0.77	8.0	15	78
E2	2.0	0.70	0.79	7.5	15	76
E5	5.0	1.73	0.78	6.0	15	69
E10	10	3.63	0.78	6.4	15	75

40 μL aluminium oxide crucibles and measured under a nitrogen atmosphere in a temperature range of −20 to 200 °C with heating and cooling rates of 10, 15, 20 and 25 K min^{-1}. The first heating curves were used to remove the thermal history, and the other curves were analysed by extrapolating transition temperatures to a zero-heating/cooling rate. Uniaxial stress–strain experiments (tensile stress test, TST) were performed on a Linkam TST350 thermostated tensile testing system, computer controlled by a T95 LinkSys apparatus. The samples were cut into pieces of similar size (20 mm × 5 mm), heated to the isotropic state and cooled down to 45 °C within 2 h. Uniaxial deformation was induced with a rate of 10 μm min^{-1} at 45 °C, and the corresponding X-ray scattering was performed after fast cooling to 20 °C. True stress is calculated for each sample and plotted against strain $\lambda = L/L_0$. Small Angle X-ray Scattering (SAXS) experiments were performed on the cSAXS beam line (X12SA) at the Swiss Light Source (Paul Scherrer Institute, Villigen, Switzerland) at an energy of 11.2 keV ($\lambda = 0.111$ nm) with a q-range of 0.01 to 1 nm^{-1} ($q = 4\pi\sin\theta/\lambda$), where 2θ is the scattering angle. Additional Small and Wide Angle X-ray Scattering (SAXS and WAXS) experiments were performed on a Rigaku MicroMax-002+ microfocused beam (4 kW, 45 kV, 0.88 mA) with the wavelength $\lambda_{Cu\text{-}K\alpha} = 0.15419$ nm. The 2D scattering patterns were collected using a Fujifilm BAS-MS 2025 imaging plate system (15.2 × 15.2 cm^2, 50 μm resolution) and a 2D Triton-200 X-ray detector (20 cm diameter). Thus the effective scattering vector q was extended from 0.01 nm^{-1} to 25 nm^{-1}. The scattering profiles were integrated after subtraction of the baseline and normalised to the mesogen peak. For the SAXS azimuthal intensity distribution a Lorentzian fitting was applied, while for MAXS and WAXS azimuthal intensity distributions, a Pseudo-Voigt fitting was used. Magnetic hysteresis properties were measured on a PMC MicroMag 3900 vibrating sample magnetometer (VSM) in fields from $B = -1$ T to 1 T at 25 °C, and mass susceptibility on an AGICO KLY-2 susceptibility bridge using the shape-memory composites, which were stretched up to a deformation of $\lambda = 2.0$. Polarized Optical Microscopy (POM) images were taken on a Leica DM LB optical microscope equipped with a Linkam CSS450 hot stage.

Results and discussion

To tailor the magnetic performance of the LCE nanocomposites, all synthetic steps were carefully done according to previously published methods[30–39] and are discussed in detail in the ESI.† The compositions and the properties of all LCE nanocomposites obtained are summarized in Table 1. An increasing dark red colour of the composites indicated the increased NP content from 0.5 to 10 w/w% as shown in Fig. 1a. The dispersion and distribution quality of the particles in the network was probed using TEM experiments, which showed little tendency for aggregation independent of the NP content (Fig. 1b and c). Insights into the crosslinking quality and determination of the gel content were achieved from swelling/deswelling experiments with chloroform/acetone (Table 1). The gel content G is defined as the weight ratio between the final solid material (after solvent extraction of the un-crosslinked components) and its initial weight. The values obtained indicate that the crosslinking was successful in all cases and similar to the reference sample (E0) with gel contents around 80%.

The swelling parameter Q (Table 1) represents the volume ratio of swollen to dry elastomer. The reference sample E0 had a swelling parameter of $Q_0 = 9.5$ which decreases with increasing nanoparticle content to values of 6.4 for E10. The trend in the

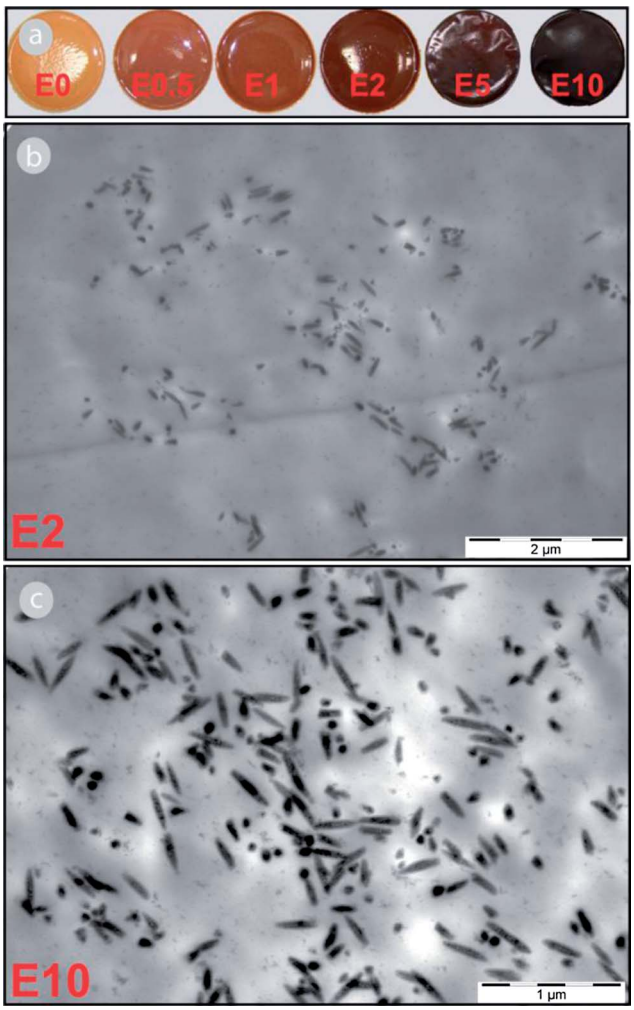

Fig. 1 (a) Images of the liquid-crystalline elastomer and liquid-crystalline elastomer nanocomposites, and (b and c) transmission electron microscopy images of the liquid-crystalline elastomer nanocomposites E2 and E10.

swelling parameter indicates an increasing crosslinking density when the particle content is increased. This effect as a function of incorporated particle content was already found also in other nanocomposite networks,[38] and can be interpreted by the covalent attachment of the NPs to the polymer matrix. Thus, increasing the nanoparticle content increases the overall crosslinking density in the final hybrid.

In order to evaluate the influence of the particles on the thermodynamic properties of the liquid-crystalline phase behaviour, DSC experiments were performed (Table 1). The uncrosslinked liquid-crystalline polymer P0 had a glass transition temperature of $T_g = 8$ °C, an endothermic peak related to the symmetry breaking at $T_{SmC-SmA} = 45$ °C, and the isotropization temperature at $T_{SI} = 110$ °C.[40] POM images confirmed the presence of both mesophases (Fig. ESI-1†). Bâtonnet texture was obtained upon cooling the liquid-crystalline polymer from the isotropic phase, and the presence of the SmA phase was confirmed at 100 °C. This SmA texture developed into a focal conic texture upon annealing, which is also characteristic of SmA phases. Finally, upon cooling below the transition temperature $T_{SmC-SmA}$, the homeotropic dark areas seen in the SmA textures were slowly lost which indicated the presence of the SmC phase. When the crosslinker was introduced, a decrease in the transition temperature T_{SI} was found due to the increased number of defects that are covalently attached to the liquid-crystalline material. The weak endothermic peak from the liquid-crystalline polymer ($T_{SmC-SmA}$) was not observed for any LCE because this was presumably diminished to levels below DSC resolution. The glass transition temperature showed an upshift in temperature from 8 to 15 °C when the liquid-crystalline polymer was crosslinked. This increase in the T_g can again be explained by the increased crosslinking density, which results in reduced free volume associated with dangling end-groups in the elastomer network.[41] For all LCE nanocomposites, similar glass transition temperatures of T_g = 15 °C and clearing temperatures of $T_{SI} = 76$ °C were found. Uniaxial stress–strain measurements were performed in combination with SAXS and WAXS experiments in order to obtain more information about the phase behaviour, the mechanical properties, and the mechanical–magnetic coupling. In Fig. 2, the stress–strain curves for all the LCEs (E0, E0.5, E1, E2, E5, E10) are shown. All materials behave similarly, independent of their particle loading, and achieve a maximal stretching of at least 350% ($\lambda = 4.5$) (Fig. 2a). In order to get a more detailed understanding of the material, the initial stress–strain curves up to $\lambda = 2$ are compared in Fig. 2b. The behaviour of the neat LCE E0 shows three different regions with regard to the local slope $d\sigma/d\lambda$ at different strain values (λ), which have also been described for other smectic LCEs.[29] In region I, the slope $d\sigma/d\lambda$ is quite steep and constantly decreasing. The region has been related to microstructural breaking of weak interactions of polymer chains to enable the deformation. In region II, the slope $d\sigma/d\lambda$ is reaching a local minimum, related to the smooth reorientation of the domains into a preferred oriented direction. In region III, the slope $d\sigma/d\lambda$ is increasing again

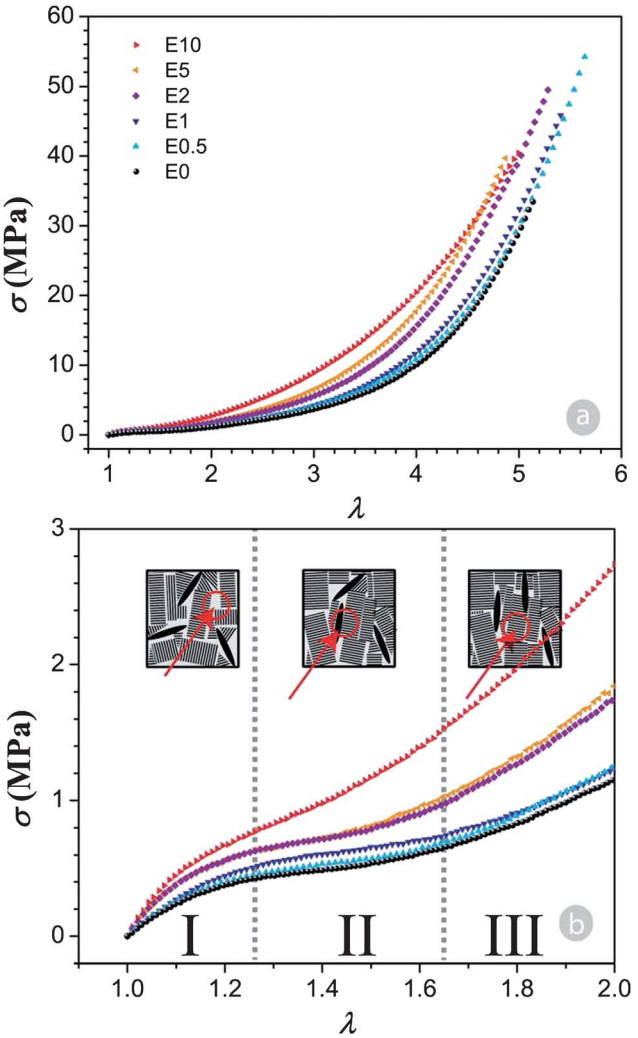

Fig. 2 (a) Uniaxial stress–strain curves for the liquid-crystalline elastomer and nanocomposites. (b) Zoom-in at the initial strain values. The inset shows the model for the reorientation processes in the three regions I, II and III.

until the elastomer breaks; in this region the polymer backbones are effectively stretched and therefore the oriented liquid-crystalline domains deform.[29] These three regions were also observed for the LCE nanocomposites (E0.5, E1, E2, E5, E10). In order to study the effect of the incorporated NPs on the nonlinear behaviour of the elastic modulus, the slope $d\sigma/d\lambda$ was calculated at different strain values λ, and plotted against the particle volume fraction ϕ_p for different stretching ratios λ (Fig. 3a). To have a quantitative measure of the composite modulus $(d\sigma/d\lambda)_c$, the Halpin–Tsai approach[28] was used, which combines the rule of mixture and the inverted rule of mixture with a coupling parameter ξ (eqn (1)):

$$\frac{\left(\frac{d\sigma}{d\lambda}\right)_c}{\left(\frac{d\sigma}{d\lambda}\right)_m} = \frac{1 + \xi\eta\phi_p}{1 - \eta\phi_p} \quad (1)$$

Here $(d\sigma/d\lambda)_m$ is the modulus of the polymer matrix and ϕ_p is the NP volume fraction. The parameter η is defined as:

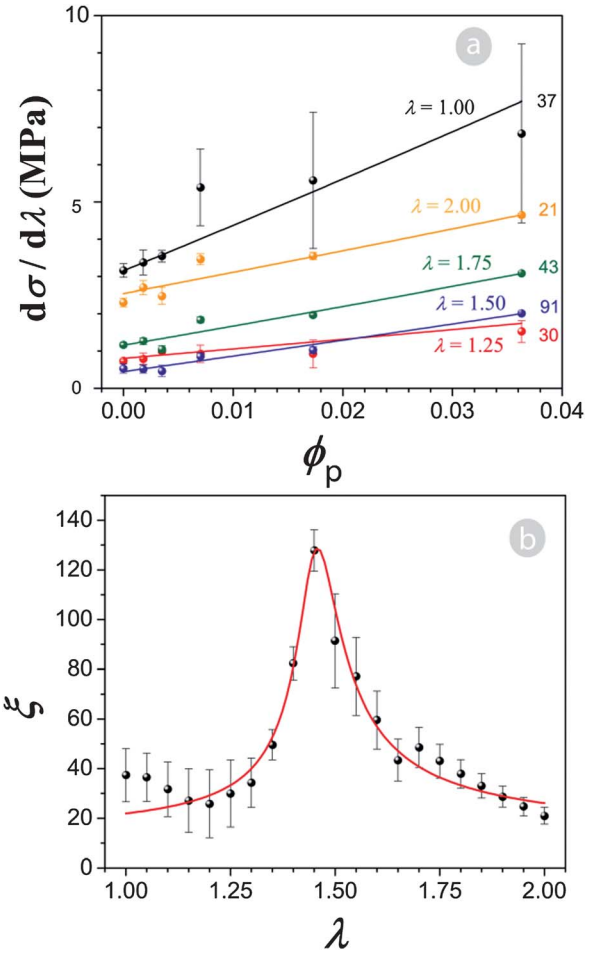

Fig. 3 (a) Evaluation of the slope $d\sigma/d\lambda$ from the uniaxial stress–strain curves as a function of the nanoparticle content ϕ_p at different strain values λ. The numbers are the values for the Halpin–Tsai coupling parameter ξ obtained from the fitting. (b) Halpin–Tsai coupling parameter ξ as a function of the applied strain λ; the curve is a guide to the eye.

$$\eta = \left(\frac{\left(\frac{d\sigma}{d\lambda}\right)_p}{\left(\frac{d\sigma}{d\lambda}\right)_m} - 1\right)\left(\frac{\left(\frac{d\sigma}{d\lambda}\right)_p}{\left(\frac{d\sigma}{d\lambda}\right)_m} + \xi\right)^{-1} \quad (2)$$

where $(d\sigma/d\lambda)_p$ is the modulus of the NPs.

For $\xi \to 0$ the design limit is the inverted rule of mixture. Thus, both components in the nanocomposite share equal stress values while deforming differently, and nanoparticles couple weakly to the matrix:

$$\lim_{\xi\to 0}\left(\frac{d\sigma}{d\lambda}\right)_c^{-1} = \left(\frac{d\sigma}{d\lambda}\right)_p^{-1}\phi_p + \left(\frac{d\sigma}{d\lambda}\right)_m^{-1}(1-\phi_p) \quad (3)$$

When $\xi \to \infty$, the design limit is the rule of mixture. Thus, both components in the nanocomposite share equal applied deformation with respect to their volume ratio and the NPs strongly couple to the matrix:

$$\lim_{\xi\to \infty}\left(\frac{d\sigma}{d\lambda}\right)_c = \left(\frac{d\sigma}{d\lambda}\right)_p\phi_p + \left(\frac{d\sigma}{d\lambda}\right)_m(1-\phi_p) \quad (4)$$

An increase in the coupling parameter ξ in this approach therefore indicates enhanced interaction of the NPs and the matrix. When this model is applied to a family of stress–strain curves from $1 < \lambda < 2$ in steps of 0.05, the ξ parameter is extracted by fitting eqn (1) and (2) and is plotted against the applied strain λ (Fig. 3b). For the NPs, an iron-oxide modulus of 200 GPa was assumed – which is a common value for inorganic fillers – which allows treating fillers essentially as non-deformable in the model.

In Fig. 3b, three regions can be distinguished as already observed for the stress–strain curves. In the initial region, the ξ parameter stays stable around $\xi = 30$. In the second region from $\lambda = 1.30$ to 1.65, the ξ parameter increases and reaches a maximum of $\xi = 130$ at $\lambda = 1.45$. In the third region, starting around $\lambda = 1.65$, the ξ parameter goes back to its original value of $\xi = 30$.

In order to explain this behaviour, the properties of the neat LCE should be recalled.[29] In the first region, weak interactions in the polymer have to be disrupted, and the relaxed non-oriented liquid-crystalline polymer chains absorb energy to enable the deformation. The NP effect in this region is less pronounced, because energy can be dissipated efficiently within the matrix. In the second region, enough stress is available and domain reorientation is the dominant process.[29] In this region, the particle effect is most prominent, and particles contribute to elongation *via* a re-orientation process coupled to the reorientation of the LCE domains. In the third region, the majority of liquid-crystalline domains have already been oriented into a monodomain, and the polymer backbone has to be stretched.[29] In view of the many orders of magnitude difference between Young moduli of NPs and LCE, a decreased coupling of the particles from the matrix in this region has to be expected. Indeed the overall material deformation can no longer be entirely sustained by particle reorientation on the inorganic side, a large amount of particles being already oriented. Thus, the only possible way to allow large deformation to progress is to decrease the coupling of NPs and the matrix, approaching a situation similar to what described by eqn (3), and allowing the organic matrix to sustain, alone, the imposed large deformations. It has to be noticed that there is no indication that the NP orientation order is having a dominant effect on the tensile strength, and continuous orientation is assumed in these regions. More details will be presented elsewhere.

X-ray scattering experiments were performed on the LCEs (E0, E0.5, E1, E2, E5, E10) at three different stretching values (λ = 1.0, 2.0, and 4.5) in order to analyse the microstructural changes in the samples. The 2D small and wide angle X-ray scattering (SAXS and WAXS) patterns of the elastomers E0, E2 and E10 are shown in Fig. 4, representatively.

The corresponding radial scattering distributions, plotted in Fig. ESI-2a–c,† allow identifying three different scattering features. In the low q region, at $q = 0.153$ nm^{-1}, an increase in scattering intensity is observed which is related to the form factor of the NPs.[19,37,38,42,43] At $q = 2.7$ to 3.7 nm^{-1}, a scattering maximum is present which corresponds to the smectic layering of the mesogens,[40] and a peak at $q = 14.4$ nm^{-1} indicates the characteristic mesogen-to-mesogen distance within a layer.

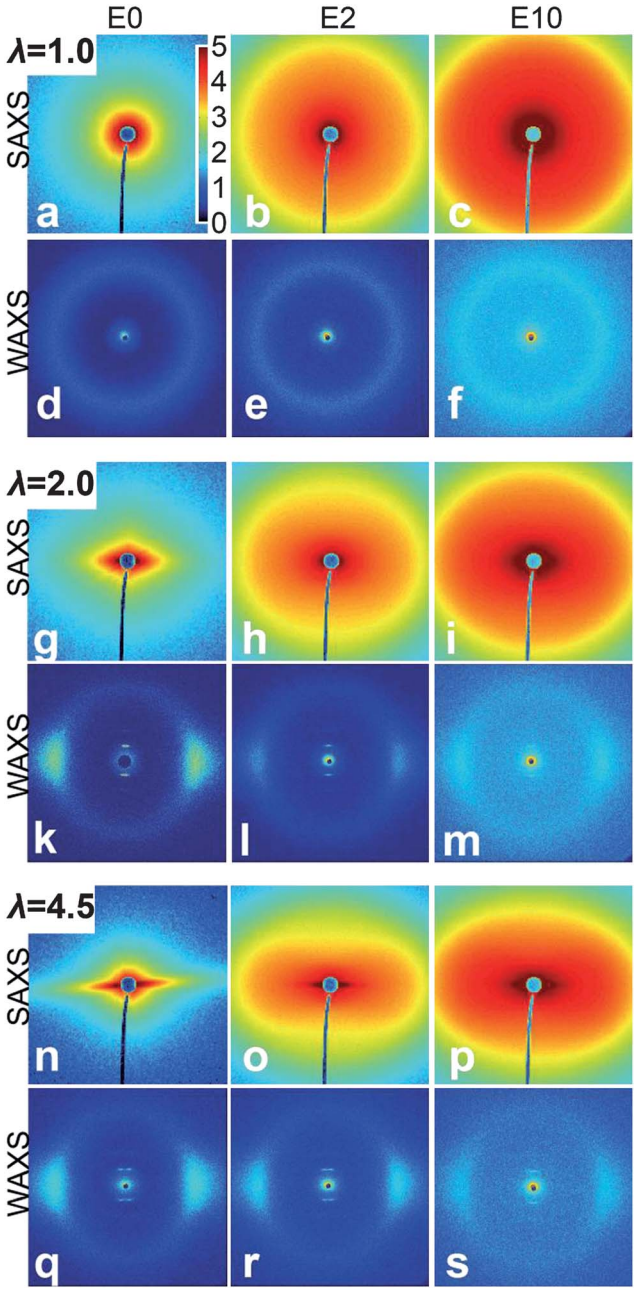

Fig. 4 2D small and wide angle X-ray scattering patterns at $\lambda = 1.0$ (a–f), $\lambda = 2.0$ (g–m), and $\lambda = 4.5$ (n–s), for the liquid-crystalline elastomer E0 and the nanocomposites E2 and E10. The intensity false colour relationship is provided in panel (a) in the logarithmic scale.

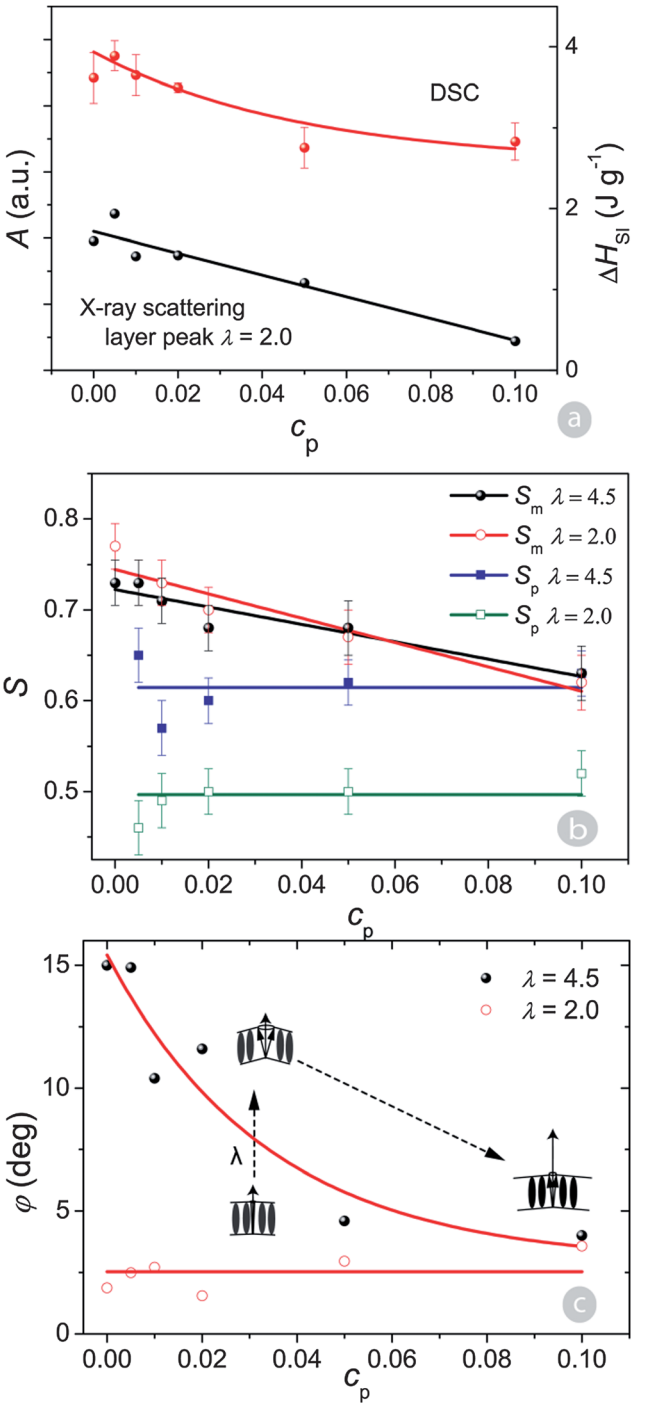

Fig. 5 (a) Area of the smectic layering peaks at $\lambda = 2.0$ and enthalpy of isotropization ΔH_{SI} as a function of the particle content c_p. (b) The mesogen S_m and nanoparticle S_p order parameter as a function of the particle content c_p at the strain values of $\lambda = 2.0$ and $\lambda = 4.5$. (c) The tilt angle of the smectic layering φ at the strain values of $\lambda = 2.0$ and $\lambda = 4.5$. The corresponding cone angles of 2.5°, 15° and 5° are sketched. Curves are guides to the eye.

Only diffuse scattering is observed in the smectic layering distance at $\lambda = 1.0$ (Fig. ESI-2a†). This is an indication of the disorder which was induced during the crosslinking of the liquid-crystalline polymer into the polydomain LCE network. At $\lambda = 2.0$, the smectic layering peak appears at $q = 3.23$ nm^{-1} (Fig. ESI-2b†). The peak area, which is normalized to the mesogen–mesogen peak, is plotted in Fig. 5a as a function of the NP content. This smectic layering peak decreases in intensity with increasing particle content from E0 to E10. From the DSC experiments, the transition enthalpies at the clearing temperature, normalized to the mass of LCE, are evaluated and added to Fig. 5a. In function of the increasing particle content, from E0 to E10, there is a tendency to decreasing enthalpy and thus, to decreasing liquid-crystalline order, which is in agreement with the trends on the reduction of the smectic layering peak.

In order to further investigate this effect, the azimuthal scattering intensity distribution was evaluated at $\lambda = 2.0$ (Fig. ESI-3†) and $\lambda = 4.5$ (Fig. ESI-4†), and the order parameter was calculated for the mesogens and for the nanoparticles directly from the azimuthal scattering profile using:[44–46]

$$S = \frac{1}{2}\frac{\int_0^{\pi/2} I(\theta)\langle 3\cos^2\theta - 1\rangle \sin\theta \mathrm{d}\theta}{\int_0^{\pi/2} I(\theta)\sin\theta \mathrm{d}\theta}. \quad (5)$$

At $\lambda = 1.0$, all azimuthal scattering patterns show isotropic scattering distributions with no orientation of either the mesogens or the NPs. At $\lambda = 2.0$ and $\lambda = 4.5$, anisotropic azimuthal scattering distributions were observed with characteristic scattering maxima that indicated preferred mesogen orientation at $q = 14.4\ \mathrm{nm}^{-1}$ (Fig. ESI-3a and ESI-4a†), and particle orientation at $q = 0.153\ \mathrm{nm}^{-1}$ (Fig. ESI-3c and ESI-4c†), both parallel to the stretching direction. For the mesogen correlation peak at $\lambda = 2.0$, a high order parameter was obtained for the reference LCE E0 ($S_m = 0.77$), which was slightly decreased with increasing particle content (E0.5, E1, E2, E5, E10) to an order parameter of around $S_m = 0.65$ (Fig. 5b). At $\lambda = 4.5$, the corresponding order parameter of the mesogen correlation peak (Fig. 5b) was decreased from $S_m = 0.73$ (E0) to $S_m = 0.63$ (E10) with increasing particle content. There was no significant difference in the mesogenic order at $\lambda = 2.0$ and 4.5, which is in agreement with previous findings for LCEs.[29]

For the particle orientation distribution at $\lambda = 2.0$, a constant characteristic order parameter around $S_p = 0.5$ was found independent of the loading for all the elastomer nanocomposites (E0.5, E1, E2, E5, E10), which is expected since no particle percolation is observed at these relatively low volume ratios; these results are indeed supported by similar studies.[47] For the nanoparticle orientation distribution at $\lambda = 4.5$, an order parameter around $S_p = 0.61$ was found. Unlike the liquid-crystalline moieties, the NP order keeps increasing with further deformation. The reorientation of the particles, however, in principle can also disturb the liquid-crystalline order and thus, be responsible for the decreasing order parameter of the liquid-crystalline phase, as presented in a study on low molecular weight nematic phases.[48]

The azimuthal peak intensity distribution (Fig. ESI-3b and ESI-4b†) of the smectic layering was deconvoluted into four overlapping peaks, and the corresponding tilt angle was calculated (Fig. 5c). For all the LCE samples (E0.5, E1, E2, E5, E10) at $\lambda = 2.0$, a tilt angle $\varphi = 2.5°$ was found which was in agreement with the findings for the liquid-crystalline polymer close to the SmC–SmA transition temperature ($T_{SmC–SmA} = 48$ °C).[40] However, at $\lambda = 4.5$, the SmC layer tilt angle φ is a function of the particle loading. A tilt angle of $\varphi = 15°$ was observed for the reference LCE E0 with four clearly separated peaks, which is similar to the tilt angle of $\varphi = 16°$ shown for the liquid-crystalline polymer at room temperature.[40] Temperature sensitive tilt angles in SmC phases have been described by de Vriess.[49] After strong deformation, also the SmA phase symmetry breaks into tilted phases due to layer undulation.[50]

In this study, the SmC layer tilt angle changes as a function of the applied deformation λ. With increasing network deformation, the shearing of the polymer backbones induces the tilt angle, a phenomenon known from similar systems.[51,52] The smectic layer tilt angle φ gradually decreases with increasing particle content from $\varphi = 15°$ to $\varphi = 4°$ for E0.5 to E10, respectively (Fig. 5b). This indicates that the decreased mobility in the polymer chains due to the particle surface effect prevents the long-range relaxation of the deformed material. This is affecting the state of order, and thus the layer organisation.

In summary, the incorporation of NPs into the LCE matrix has an effect on the microstructure of the material. Increasing the particle fraction up to a volume ratio of 3.6 v/v% decreases the organisation of the mesogen moieties into the smectic layers and prevents effective relaxation of the polymer into the most stable conformations due to reduced polymer mobility. However, the smectic layering is preserved in the nanocomposites similarly to the nanocomposites of the liquid-crystalline polymer[53] and the shape-memory properties are also preserved in the LCE nanocomposites.[19]

According to the SAXS experiments, also the NPs reoriented during the uniaxial deformation. This fact, together with earlier findings[19,54] and the Stoner–Wohlfarth theory,[55] suggests that these LCE nanocomposites should display anisotropy in their magnetic properties, depending on the strain and nanoparticles content.

To verify whether all the assumptions of Stoner and Wohlfarth can be applied to our systems, and to gain further insight into the magnetic domain structure of the nanocomposites, analysis of first-order reversal curves (FORC) was carried out for E10, because the highest distortion would be expected here due to the high nanoparticle concentration. The FORCs were measured using either a 0.1 s or 2 s averaging time in order to investigate relaxation effects (Fig. ESI-5†). From these measurements, it can be seen that part of the hysteresis signal arises from the reversible magnetization of the non-ferromagnetic material (Fig. ESI-5a and b†), *i.e.* the liquid-crystal. The signal of the irreversible part, which is coming from the iron oxide, proves the absence of particle interaction. Thus, the derivative of the remanence curve (Fig. ESI-5a and b†) and the narrow interaction field in the FORC distribution are in agreement (Fig. ESI-5c and d†). As reversible and irreversible parts of the magnetization appear at the same field, thermal relaxation is found not important; thus, no superparamagnetic behaviour is found. Consequently, from the measurements with different relaxation times, the observed behaviour is almost identical (Fig. ESI-5e and f†). The dominance of low coercivity (peaked at <4 kA m^{-1}) is typical for maghemite in the particle size of the nanoparticles.

In summary, the bulk of the soft ferrimagnetic material is magnetically ordered and the shape of the individual magnetic particle is responsible for its magnetic properties. Thus, the orientation distribution function of all particles dominates the magnetic properties of the macroscopic sample, fulfilling the assumptions of Stoner and Wohlfarth as a proof of concept.

In order to evaluate the magnetic features for potential applications, magnetic susceptibility and hysteresis were

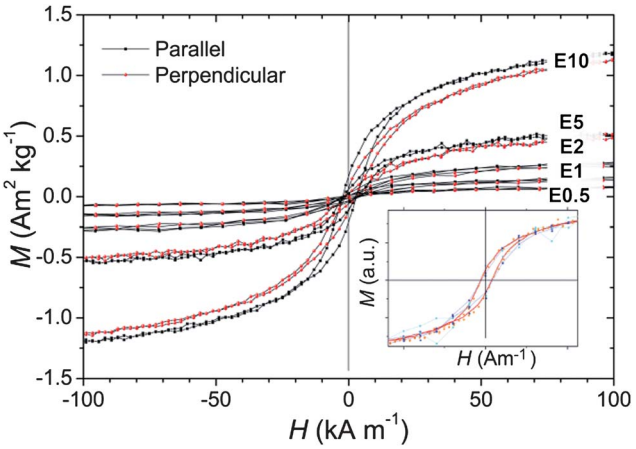

Fig. 6 Magnetisation curves (measured parallel and perpendicular to the director) of the liquid-crystalline elastomer nanocomposites E0.5–E10 in the low-field region. The inset shows the superposition to a master curve after normalization to the saturation magnetisation M_s.

measured on all samples (E0, E0.5, E1, E2, E5, E10) for the deformation value of $\lambda = 2.0$, both parallel and perpendicular to the orientation of stretching (Fig. 6). The transformation from the NP random orientation distribution at $\lambda = 1.0$ to the oriented ones was derived earlier for the susceptibility values of E10.[19] For the reference sample E0, the magnetisation response M of the LCE was below the detection limit. For the nanocomposites, normalizing the loops to the saturation magnetization shows the same hysteretic behaviour for all the samples (Fig. 6, inset).

The saturation magnetization M_s was reached independent of the orientation of the particles, and a linear increase in M_s with increased particle loading was observed (Fig. 7a). A similar increase is seen in the remanent magnetization M_r with increased loading (Fig. 7b). Comparing the two directions, parallel and perpendicular to the particle orientation, $M_{r\parallel}$ is about 1.9 times higher than $M_{r\perp}$. This is a direct consequence of the particle orientation and it is explained in terms of the Stoner–Wohlfarth model and the demagnetizing factors for magnetic ellipsoids.[55]

In Fig. 7c, the magnetic susceptibilities $\chi_\parallel$ and $\chi_\perp$ of all magnetic LCE nanocomposites are shown, and an average value for the magnetic susceptibility anisotropy of $\chi_\parallel/\chi_\perp = 1.6$ was found for all samples in qualitative agreement with a previous, more detailed study centred on the sample E10.[19] The magnetization ratio M_r/M_s (Fig. 7d) and the coercivity H_c (Fig. 7e) are invariant to the particle loading. This again proves both, that the particles are well dispersed and do not interact, and that the composition of the ferrimagnetic particles does not change with increasing loading, which is also supported by the normalized hysteresis loops.[55–57] There is also a significant anisotropy of the coercive field. In theory, independent of the population of particles at an orientation angle θ, any non-zero population value should generate an identical coercive field in the direction of the shape-anisotropic particle orientation, according to the Stoner–Wohlfarth theory.[55] Thus, the measurement of the coercive field is in agreement with the evaluation of the SAXS

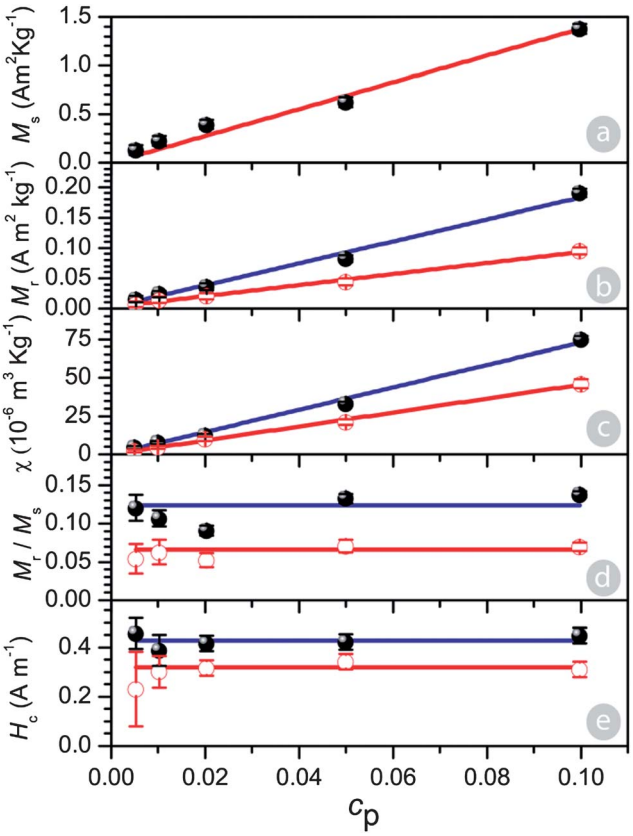

Fig. 7 (a) Saturation magnetisation M_s, (b) remanent magnetisation M_r, (c) magnetic susceptibility χ, (d) normalised remanent magnetisation M_r/M_s, and (e) magnetic coercivity H_c as a function of the particle content c_p for the liquid-crystalline elastomer nanocomposites E0.5–E10. Full symbols represent parallel, empty symbols perpendicular measurements. For the saturation, the orientation-independent average is shown.

patterns and supports the assumption of negligible orientation of the nanoparticles in the direction perpendicular to the uniaxial deformation.

Conclusions

In this work, magnetic nano-ellipsoids were coupled to a soft shape-memory liquid-crystalline matrix for the construction of reshapeable and deformable soft magnets. In a concentration series from 0.5 to 10 w/w% of anisotropic magnetic nanoparticles, the structural, mechanical and magnetic properties were analysed. After uniaxial deformation, anisotropy was found for the magnetic susceptibility, the magnetic coercivity and the remanent magnetisation, and these were correlated with the particle shape and their orientation distribution which was obtained from X-ray diffraction experiments. In tensile tests, the effect of particles on the modulus of the material was evaluated and three different regions were found. The most effective modulus increase occurred in the softening region of the nanocomposite. In combination with the microstructure analysis from X-ray scattering experiments, further insight into the stabilization effect of elastomer–nanoparticle interactions was obtained and a model for the hardening of the LCE at increasing nanoparticle content was proposed. These results demonstrate that by carefully adjusting the chemistry and

composition of the building blocks of liquid-crystalline elastomer–nanoparticle composites, optimized magnetic properties can be obtained without jeopardizing the microstructure of the liquid-crystalline matrix, and that both features can be combined to open new opportunities in applications such as strain sensors, sensitive actuators and magnetic switches.

Acknowledgements

We gratefully acknowledge financial support from the Adolphe Merkle Foundation, ETH Zurich and thank the Swiss National Science Foundation NRP62 "Smart Materials" for funding this project. The SAXS measurements were performed with the appreciated help of Dr Jérôme. J. Crassous on the cSAXS beamline (X12SA) of the Swiss Light Source at the Paul Scherrer Institute, Villigen, Switzerland, and we kindly acknowledge the expert help from our local contact Dr Teemu Ikonen.

Notes and references

1 M. Warner and E. M. Terentjev, *Liquid Crystal Elastomer*, Oxford University Press, Oxford, 2007.
2 J. S. Biggins, M. Warner and K. Bhattacharya, *J. Mech. Phys. Solids*, 2012, **60**, 573–590.
3 C. Ohm, M. Brehmer and R. Zentel, *Adv. Mater.*, 2010, **22**, 3366–3387.
4 A. Sánchez-Ferrer, T. Fischl, M. Stubenrauch, H. Wurmus, M. Hoffmann and H. Finkelmann, *Macromol. Chem. Phys.*, 2009, **210**, 1671–1677.
5 A. Sánchez-Ferrer, T. Fischl, M. Stubenrauch, A. Albrecht, H. Wurmus, M. Hoffmann and H. Finkelmann, *Adv. Mater.*, 2011, **23**, 4526–4530.
6 V. Domenici, M. Conradi, M. Remškar, M. Viršek, B. Zupančič, A. Mrzel, M. Chambers and B. Zalar, *J. Mater. Sci.*, 2011, **46**, 3639–3645.
7 M. Chambers, H. Finkelmann, M. Remškar, A. Sánchez-Ferrer, B. Zalar and S. Žumer, *J. Mater. Chem.*, 2009, **19**, 1524–1531.
8 R. Montazami, C. M. Spillmannm, J. Naciri and B. R. Ratna, *Sens. Actuators, A*, 2012, **178**, 175–178.
9 Y. Ji, Y. Y. Huang, R. Rungsawang and E. M. Terentjev, *Adv. Mater.*, 2010, **22**, 3436–3440.
10 B. Pradhan, K. Setyowati, H. Liu, D. H. Waldeck and J. Chen, *Nano Lett.*, 2008, **8**, 1142–1146.
11 H. Koerner, G. Price, N. A. Pearce, M. Alexander and R. A. Vaia, *Nat. Mater.*, 2004, **3**, 115–120.
12 C. Weder, *J. Mater. Chem.*, 2011, **21**, 8235.
13 L. Hsu, C. Weder and S. J. Rowan, *J. Mater. Chem.*, 2010, **21**, 2812–2822.
14 J. Jestin, F. Cousin, I. Dubois, C. Ménager, R. Schweins, J. Oberdisse and F. Boué, *Adv. Mater.*, 2008, **20**, 2533–2540.
15 D. Collin, G. K. Auernhammer, O. Gavat, P. Martinoty and H. R. Brand, *Macromol. Rapid Commun.*, 2003, **24**, 737–741.
16 M. Y. Razzaq, M. Behl and A. Lendlein, *Nanoscale*, 2012, **4**, 6181–6195.
17 A. Kaiser, M. Winkler, S. Krause, H. Finkelmann and A. M. Schmidt, *J. Mater. Chem.*, 2009, **19**, 538–543.
18 A. Garcia-Márquez, A. Demortière, B. Heinrich, D. Guillon, S. Bégin-Colin and B. Donnio, *J. Mater. Chem.*, 2011, **21**, 8994–8996.
19 J. M. Haberl, A. Sánchez-Ferrer, A. M. Mihut, H. Dietsch and R. Mezzenga, *Adv. Mater.*, 2013, **25**, 1787–1791.
20 I. A. Rousseau and P. T. Mather, *J. Am. Chem. Soc.*, 2003, **125**, 15300–15301.
21 J. R. Potts, O. Shankar, L. Du and R. S. Ruoff, *Macromolecules*, 2012, **45**, 6045–6055.
22 A. Papon, H. Montes, M. Hanafi, F. Lequeux, L. Guy and K. Saalwächter, *Phys. Rev. Lett.*, 2012, **108**, 065702.
23 A. Papon, H. Montes, F. Lequeux, J. Oberdisse, K. Saalwächter and L. Guy, *Soft Matter*, 2012, **8**, 4090–4096.
24 F. W. Starr, T. B. Schröder and S. C. Glotzer, *Macromolecules*, 2002, **35**, 4481–4492.
25 J. F. Douglas and K. F. Freed, *Macromolecules*, 1997, **30**, 1813–1817.
26 S. Merabia, P. Sotta and D. R. Long, *Macromolecules*, 2008, **41**, 8252–8266.
27 H. Denver, T. Geiman, E. Martin, A. Gupta and D.-A. Borca-Tasciuc, *J. Appl. Phys.*, 2009, **106**, 064909.
28 J. C. Halpin and J. L. Kardos, *Polym. Eng. Sci.*, 1976, **16**, 344–352.
29 A. Sanchez-Ferrer and H. Finkelmann, *Macromol. Rapid Commun.*, 2011, **32**, 309–315.
30 M. Ocaña, M. P. Morales and C. J. Serna, *J. Colloid Interface Sci.*, 1999, **212**, 317.
31 C. Rufier, M. Reufer, H. Dietsch and P. Schurtenberger, *Langmuir*, 2011, **27**, 6622–6627.
32 C. Graf, D. L. J. Vossen, A. Imhof and A. van Blaaderen, *Langmuir*, 2003, **19**, 6693–6700.
33 T. Chappuis, I. Bobowska, S. Hengsberger, E. Vanoli and H. Dietsch, *Chimia*, 2011, **65**, 979–981.
34 F. Vereda, J. de Vicente and R. Hidalgo-Álvarez, *ChemPhysChem*, 2009, **10**, 1165–1179.
35 M. Reufer, H. Dietsch, U. Gasser, B. Groberty, A. M. Hirt, V. K. Malik and P. Schurtenberger, *J. Phys.: Condens. Matter*, 2011, **23**, 065102.
36 L. Zadoina, B. Lonetti, K. Soulantica, A.-F. Mingotaud, M. Respaud, B. Chaudret and M. Mauzac, *J. Mater. Chem.*, 2009, **19**, 8075–8078.
37 A. Sanchez-Ferrer, M. Reufer, R. Mezzenga, P. Schurtenberger and H. Dietsch, *Nanotechnology*, 2010, **21**, 185603.
38 A. M. Mihut, A. Sánchez-Ferrer, J. J. Crassous, L. Ackermann Hirschi, R. Mezzenga and H. Dietsch, *Polymer*, 2013, submitted.
39 A. Sánchez-Ferrer, D. Rogez and P. Martinoty, *Macromol. Chem. Phys.*, 2010, **211**, 1712–1721.
40 A. Martínez-Gómez, E. Pérez and A. Bello, *Colloid Polym. Sci.*, 2010, **288**, 859–867.
41 A. Hale, C. W. Macosko and H. E. Bair, *Macromolecules*, 1991, **24**, 2610–2621.
42 M. Reufer, H. Dietsch, U. Gasser, A. Hirt, A. Menzel and P. Schurtenberger, *J. Phys. Chem. B*, 2010, **114**, 4763–4769.
43 A. Sánchez-Ferrer, R. Mezzenga and H. Dietsch, *Macromol. Chem. Phys.*, 2011, **212**, 627–634.

44 R. Lovell and G. R. Mitchell, *Acta Crystallogr., Sect. A: Cryst. Phys., Diffr., Theor. Gen. Crystallogr.*, 1981, **37**, 135–137.
45 G. R. Mitchell and A. H. Windle, in *Developmentin Crystalline Polymers-2*, ed. D. C. Basset, Elsevier Applied Science, London, 1988, vol. 3, p. 115.
46 J. J. Hermans, P. H. Hermans, D. Vermaas and A. Weidinger, *Recl. Trav. Chim. Pays-Bas*, 1946, **65**, 427–447.
47 N. Chemin, L. Rozes, C. Chanéac, S. Cassaignon, E. Le Bourhis, J.-P. Jolivet, O. Spalla, E. Barthel and C. Sanchez, *Chem. Mater.*, 2008, **20**, 4602–4611.
48 S. Hernàndez-Navarro, P. Tierno, J. Igneés-Mullol and F. Sagués, *Soft Matter*, 2011, **7**, 5109–5112.
49 A. de Vries, *Mol. Cryst. Liq. Cryst.*, 1977, **41**, 27–31.
50 E. Nishikawa and H. Finkelmann, *Macromol. Chem. Phys.*, 1999, **200**, 312–322.
51 A. Sánchez-Ferrer and H. Finkelmann, *Mol. Cryst. Liq. Cryst.*, 2009, **508**, 348–356.
52 A. Sánchez-Ferrer and H. Finkelmann, *Macromolecules*, 2008, **41**, 970–980.
53 A. Martínez-Gómez, E. Pérez and C. Álvarez, *Polymer*, 2009, **50**, 1447–1455.
54 Y. Watanabe, *J. Compos. Mater.*, 2002, **36**(8), 915–923.
55 E. C. Stoner and E. P. Wohlfarth, *Philos. Trans. R. Soc., A*, 1948, **240**, 599–624.
56 A. B. Kulakov, I. P. Lavrent-ev and V. I. Petinov, Coercivity of Homogenized Ensembles of Anisotropic γ-Fe_2O_3 Nanoparticles, *Solid-State Electron.*, 2011, **2**, 238–244.
57 L. Schulz, W. Schirmacher, A. Omran, V. R. Shah, P. Böni, W. Petry and P. Müller-Buschbaum, *J. Phys.: Condens. Matter*, 2010, **22**, 346008–346013.